

Search for Neutrinoless β^+EC Decay of ^{120}Te with CUORE-0

C. Alduino,¹ K. Alfonso,² D. R. Artusa,^{1,3} F. T. Avignone III,¹ O. Azzolini,⁴ G. Bari,⁵ F. Bellini,^{6,7} G. Benato,⁸ A. Bersani,⁹ M. Biassoni,^{10,11} A. Branca,^{12,13} C. Brofferio,^{10,11} C. Bucci,³ A. Camacho,⁴ A. Caminata,⁹ L. Canonica,^{14,3} X. G. Cao,¹⁵ S. Capelli,^{10,11} L. Cappelli,^{8,16,3} L. Cardani,⁷ P. Carniti,^{10,11} N. Casali,⁷ L. Cassina,^{10,11} D. Chiesa,^{10,11} N. Chott,¹ M. Clemenza,^{10,11} S. Copello,^{17,9} C. Cosmelli,^{6,7} O. Cremonesi,¹¹ R. J. Creswick,¹ J. S. Cushman,¹⁸ A. D’Addabbo,³ D. D’Aguanno,^{3,19} I. Dafinei,⁷ C. J. Davis,¹⁸ S. Dell’Oro,^{20,3,21} M. M. Deninno,⁵ S. Di Domizio,^{17,9} M. L. Di Vacri,^{3,22} A. Drobizhev,^{8,16} D. Q. Fang,¹⁵ M. Faverrani,^{10,11} E. Ferri,¹¹ F. Ferroni,^{6,7} E. Fiorini,^{11,10} M. A. Franceschi,²³ S. J. Freedman,^{16,8,*} B. K. Fujikawa,¹⁶ A. Giachero,¹¹ L. Gironi,^{10,11} A. Giuliani,²⁴ L. Gladstone,¹⁴ P. Gorla,³ C. Gotti,^{10,11} T. D. Gutierrez,²⁵ K. Han,²⁶ K. M. Heeger,¹⁸ R. Hennings-Yeomans,^{8,16} H. Z. Huang,² G. Keppel,⁴ Yu. G. Kolomensky,^{8,16} A. Leder,¹⁴ C. Ligi,²³ K. E. Lim,¹⁸ Y. G. Ma,¹⁵ L. Marini,^{17,9} M. Martinez,^{6,7,27} R. H. Maruyama,¹⁸ Y. Mei,¹⁶ N. Moggi,^{28,5} S. Morganti,⁷ P. J. Mosteiro,⁷ S. S. Nagorny,^{3,21} T. Napolitano,²³ M. Nastasi,^{10,11} C. Nones,²⁹ E. B. Norman,^{30,31} V. Novati,²⁴ A. Nucciotti,^{10,11} T. O’Donnell,²⁰ J. L. Ouellet,¹⁴ C. E. Pagliarone,^{3,19} M. Pallavicini,^{17,9} V. Palmieri,⁴ L. Pattavina,³ M. Pavan,^{10,11} G. Pessina,¹¹ C. Pira,⁴ S. Pirro,³ S. Pozzi,^{10,11} E. Previtali,¹¹ C. Rosenfeld,¹ C. Rusconi,^{1,3} M. Sakai,² S. Sangiorgio,³⁰ D. Santone,^{3,22} B. Schmidt,¹⁶ J. Schmidt,² N. D. Scielzo,³⁰ V. Singh,⁸ M. Sisti,^{10,11} L. Taffarello,¹² F. Terranova,^{10,11} C. Tomei,⁷ M. Vignati,⁷ S. L. Wagaarachchi,^{8,16} B. S. Wang,^{30,31} H. W. Wang,¹⁵ B. Welliver,¹⁶ J. Wilson,¹ L. A. Winslow,¹⁴ T. Wise,^{18,32} A. Woodcraft,³³ L. Zanotti,^{10,11} G. Q. Zhang,¹⁵ S. Zimmermann,³⁴ and S. Zucchelli^{28,5}

(CUORE Collaboration)

¹Department of Physics and Astronomy, University of South Carolina, Columbia, SC 29208, USA

²Department of Physics and Astronomy, University of California, Los Angeles, CA 90095, USA

³INFN – Laboratori Nazionali del Gran Sasso, Assergi (L’Aquila) I-67100, Italy

⁴INFN – Laboratori Nazionali di Legnaro, Legnaro (Padova) I-35020, Italy

⁵INFN – Sezione di Bologna, Bologna I-40127, Italy

⁶Dipartimento di Fisica, Sapienza Università di Roma, Roma I-00185, Italy

⁷INFN – Sezione di Roma, Roma I-00185, Italy

⁸Department of Physics, University of California, Berkeley, CA 94720, USA

⁹INFN – Sezione di Genova, Genova I-16146, Italy

¹⁰Dipartimento di Fisica, Università di Milano-Bicocca, Milano I-20126, Italy

¹¹INFN – Sezione di Milano Bicocca, Milano I-20126, Italy

¹²INFN – Sezione di Padova, Padova I-35131, Italy

¹³Dipartimento di Fisica e Astronomia, Università di Padova, I-35131 Padova, Italy

¹⁴Massachusetts Institute of Technology, Cambridge, MA 02139, USA

¹⁵Shanghai Institute of Applied Physics, Chinese Academy of Sciences, Shanghai 201800, China

¹⁶Nuclear Science Division, Lawrence Berkeley National Laboratory, Berkeley, CA 94720, USA

¹⁷Dipartimento di Fisica, Università di Genova, Genova I-16146, Italy

¹⁸Department of Physics, Yale University, New Haven, CT 06520, USA

¹⁹Dipartimento di Ingegneria Civile e Meccanica,

Università degli Studi di Cassino e del Lazio Meridionale, Cassino I-03043, Italy

²⁰Center for Neutrino Physics, Virginia Polytechnic Institute and State University, Blacksburg, Virginia 24061, USA

²¹INFN – Gran Sasso Science Institute, L’Aquila I-67100, Italy

²²Dipartimento di Scienze Fisiche e Chimiche, Università dell’Aquila, L’Aquila I-67100, Italy

²³INFN – Laboratori Nazionali di Frascati, Frascati (Roma) I-00044, Italy

²⁴CSNSM, Univ. Paris-Sud, CNRS/IN2P3, Université Paris-Saclay, 91405 Orsay, France

²⁵Physics Department, California Polytechnic State University, San Luis Obispo, CA 93407, USA

²⁶INPAC and School of Physics and Astronomy,

Shanghai Jiao Tong University; Shanghai Laboratory for Particle Physics and Cosmology, Shanghai 200240, China

²⁷Laboratorio de Fisica Nuclear y Astroparticulas,

Universidad de Zaragoza, Zaragoza 50009, Spain

²⁸Dipartimento di Fisica e Astronomia, Alma Mater Studiorum – Università di Bologna, Bologna I-40127, Italy

²⁹Service de Physique des Particules, CEA / Saclay, 91191 Gif-sur-Yvette, France

³⁰Lawrence Livermore National Laboratory, Livermore, CA 94550, USA

³¹Department of Nuclear Engineering, University of California, Berkeley, CA 94720, USA

³²Department of Physics, University of Wisconsin, Madison, WI 53706, USA

³³SUPA, Institute for Astronomy, University of Edinburgh, Blackford Hill, Edinburgh EH9 3HJ, UK

³⁴Engineering Division, Lawrence Berkeley National Laboratory, Berkeley, CA 94720, USA

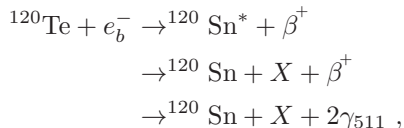
(Dated: October 23, 2017)

We have performed a search for neutrinoless β^+EC decay of ^{120}Te using the final CUORE-0 data release. We describe a new analysis method for the simultaneous fit of signatures with different event topology, and of data subsets with different signal efficiency, obtaining a limit on the half-life of the decay of $T_{1/2} > 1.6 \cdot 10^{21}$ yr at 90% CI. Combining this with results from Cuoricino, a predecessor experiment, we obtain the strongest limit to date, corresponding to $T_{1/2} > 2.7 \cdot 10^{21}$ yr at 90% CI.

I. INTRODUCTION

The search for neutrinoless double beta ($0\nu\beta\beta$) decay [1, 2] aims at answering questions regarding the conservation of total lepton number [3], the Majorana or Dirac nature of neutrinos [4], and the mechanism inducing non-zero splittings between the neutrino mass eigenvalues [5–10]. The process can consist of the emission of two electrons – which is the most commonly investigated option – or of two positrons ($0\nu\beta^+\beta^+$). In the latter case, one or both positrons can be substituted by an electron capture (EC). For $0\nu ECEC$ decay, the decay rate is typically suppressed because an additional radiative process is required by energy and momentum conservation. Hence, the $0\nu\beta^+\beta^+$ and $0\nu\beta^+EC$ decays are more interesting from the experimental perspective.

The Cryogenic Underground Observatory for Rare Events (CUORE) [11, 12] and CUORE-0 [13, 14] are experiments searching for the $0\nu\beta\beta$ decay of ^{130}Te with TeO_2 crystals operated as bolometric detectors. The use of tellurium with natural isotopic composition in the crystals also allows us to search for the decay of isotopes other than ^{130}Te . In particular, ^{120}Te , present with a natural abundance of 0.09(1)% [15], can decay via $0\nu ECEC$ and via $0\nu\beta^+EC$ disintegration. In this work, we present the search for $0\nu\beta^+EC$ decay using CUORE-0 data. At present, no calculation of the nuclear matrix element is available in literature for ^{120}Te decay. For other isotopes, the expected $0\nu\beta^+EC$ half-lives are a few orders of magnitude larger than that of $0\nu\beta\beta$ decay for the most commonly investigated cases [16, 17]. Despite this, and the low abundance of ^{120}Te , the presence of the β^+ with the consequent emission of a pair of back-to-back 511 keV γ rays provides extremely clean signatures of $0\nu\beta^+EC$ decays. The $0\nu\beta^+EC$ decay of ^{120}Te can be written as:



where e_b^- indicates the atomic electron captured from a shell with binding energy E_b , while X indicates an Auger electron or an X-ray emitted in the process. In $0\nu\beta^+EC$ decay the available energy is shared between the four emitted particles, with the daughter nucleus being almost

at rest because of its larger mass. Here, we assume that the X-ray or the Auger electron are fully absorbed in the same crystal where the decay takes place. Namely, the K-shell binding energy of tin is 29.2 keV [18]. Electrons and γ rays of this energy have a chance to escape the crystal only if they are emitted at $\lesssim 10$ μm from the surface, thus only the decays taking place in a negligible fraction of the crystal volume would be affected by energy loss.

Given the absence of neutrinos carrying away part of the available energy, the kinetic energy K of the emitted positron is peaked at $K = Q - 2m_e - E_b$, where Q is the Q-value of the reaction:

$$Q = m(^{120}\text{Te}) - m(^{120}\text{Sn}) \ , \quad (1)$$

and m are the masses of the considered nuclei. Only one direct measurement of Q , obtained with a Penning trap, is available in literature, i.e. $Q = 1714.8 \pm 1.3$ keV [19].

The energy deposited inside the crystal where the decay takes place, μ , is the sum of the kinetic energy of the positron and that of the X-ray or Auger electron. Since, in most of the cases, the positron is fully absorbed, we can write:

$$\mu = K + E_b = Q - 2m_e = 692.8 \pm 1.3 \text{ keV} \ . \quad (2)$$

The expected energy spectrum for $0\nu\beta^+EC$ decay in the detector where the process occurs is therefore a peak at μ . If we also consider the two 511 keV γ rays, six different signatures are possible. These are depicted in Fig. 1 and reported in Table I (we refer them with the symbol (s), with $s = 0, \dots, 5$). Each γ can either be absorbed in the same crystal, or in a different crystal, or escape the detector volume and be absorbed elsewhere.

The most stringent limit on ^{120}Te $0\nu\beta^+EC$ half-life, $T_{1/2} > 1.9 \cdot 10^{21}$ yr at 90% confidence level (C.L.) [20], was obtained by Cuoricino [21]. The exposure of CUORE-0 is just about half of the Cuoricino one, however the lower background and higher signal efficiency lead to a higher sensitivity. Moreover, in the present work we develop an analysis method which fully exploits the information available in all the six different $0\nu\beta^+EC$ decay signatures. These factors allow to reach a sensitivity to $0\nu\beta^+EC$ decay comparable to that of Cuoricino. CUORE will have a much higher sensitivity due primarily to the larger mass and efficiency of detecting the two 511 keV gammas.

II. CUORE-0

CUORE-0 was a prototype of CUORE operated between 2013 and 2015. In addition to being a test

* Deceased

TABLE I. Signatures of ^{120}Te $0\nu\beta^+EC$ decay in CUORE-0. For each signature (s) we report the signal peak position $\bar{\mu}$ of $0\nu\beta^+EC$ decay, the multiplicity M corresponding to the number of crystals with a non-zero energy deposition, and the fit range(s) ΔE_i , with $i = 1, \dots, M$. The range of signature (0) is narrower than all others due to the presence of shoulders at ~ 640 keV and ~ 740 keV which would require the parameterization of the continuum background with a high-order polynomial. The last two columns report the average containment efficiency ε_{MC} , i.e. the probability of having a full energy deposition in the detector volume. We obtain this from MC simulations, and report it with its relative binomial uncertainty for floors 2–12 and 1,13.

Signature	$\bar{\mu}$ [keV]	M	Energy range [keV]			$\varepsilon_{\text{MC}}[\%]$	
			ΔE_1	ΔE_2	ΔE_3	Fl. 2 – 12	Fl. 1, 13
(0)	692.8	1	[657, 720]			0.162(2)	0.309(4)
(1)	1203.8	1	[1150, 1250]			1.23(2)	1.60(2)
(2)	1714.8	1	[1665, 1775]			0.90(1)	0.92(1)
(3)	(692.8, 511)	2	[650, 750]	[460, 560]		0.317(3)	0.303(3)
(4)	(1203.8, 511)	2	[1150, 1250]	[460, 560]		0.657(5)	0.471(4)
(5)	(692.8, 511, 511)	3	[650, 750]	[460, 560]	[460, 560]	0.0559(5)	0.0196(3)

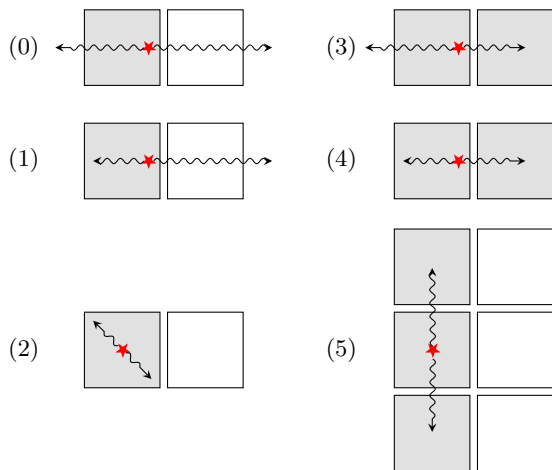


FIG. 1. Signatures of ^{120}Te $0\nu\beta^+EC$ decay in CUORE-0. The red stars represent the β^+ energy depositions, and the arrows represent the 511 keV γ rays following its annihilation. The shaded squares represent the crystals with non-zero energy depositions. We do not apply any distance cut for signatures (3)–(5) and accept also events depositing energy in non-neighboring crystals.

stand for the CUORE assembly [22] and cleaning procedures [23, 24], CUORE-0 provided data leading to competitive physics results [25, 26]. CUORE-0 consisted of 52 TeO_2 crystals with natural Te composition operated as source and detector for the $0\nu\beta\beta$ decay of ^{130}Te . The crystals are 5 cm cubes mounted in a tower of 13 floors, with 4 crystals per floor. They were operated as cryogenic calorimeters (bolometers) at a temperature of ~ 10 mK and read-out with neutron transmutation doped germanium thermistors. The total TeO_2 mass is 39 kg. Using the most recent evaluation of the ^{120}Te natural abundance, $f_{120} = 0.09(1)\%$ [15], the ^{120}Te mass contained in CUORE-0 is 28 g, corresponding to $1.3 \cdot 10^{23}$ atoms of ^{120}Te . We note that this value of f_{120} differs from the $0.096(2)\%$ used by Cuoricino [20], which was taken from Ref. [27].

CUORE-0 used the same cryostat and shielding as Cuoricino [28, 29]. The shielding consists of two external layers of low radioactivity lead for a total thickness of 20 cm and a 1.2 cm internal layer of cold ancient Roman lead [30]. The cryostat thermal shields are made of electrolytic copper which provides an additional layer of shielding (~ 1.5 cm), and the whole cryostat is enclosed in a 10 cm layer of borated polyethylene shielding. The front end electronics and the data acquisition were the same as for Cuoricino. For a more detailed description, see Refs. [13, 29, 31, 32].

III. DATA ANALYSIS

We use the entire CUORE-0 data set, which corresponds to 35.2 kg-yr of TeO_2 exposure. We use the same data processing and selection as described in Ref. [33], except for anti-coincidence cut, since we now select events with multiplicity M (i.e. numbers of crystals with a non-zero energy deposition) and energy which satisfy the criteria reported in Table I.

The application of the selection cuts introduces an efficiency term, ε_{cut} , which is common to all signatures. This is the product of the trigger and reconstruction efficiency, $\varepsilon_{\text{trigger}}$, and of the pile-up and Pulse Shape Analysis (PSA) efficiency, ε_{PSA} . We use the same values reported in [33], i.e. $\varepsilon_{\text{trigger}} = 98.529 \pm 0.004\%$ and $\varepsilon_{\text{PSA}} = 93.7 \pm 0.7\%$. The product of the two yields $\varepsilon_{\text{cut}} = 92.3 \pm 0.7\%$. We apply these cuts independently to each channel, exponentiating the efficiency term to the corresponding multiplicity: $\varepsilon_{\text{cut}}^M$.

Additionally, the selection of events with $M = 1, 2$ or 3 introduces a further efficiency term, ε_M . We exploit the CUORE-0 event rate (~ 0.001 Hz) to compute the probability of having random coincidences, which induce pile-up events in the $M = 1, M = 2$ and $M = 3$ spectra [34], obtaining the following coincidence efficiencies: $\varepsilon_{M=1} = 99(1)\%$, $\varepsilon_{M=2} = 99.2(1)\%$ and $\varepsilon_{M=3} = 98.8(1)\%$.

Finally, we consider the containment efficiency, i.e. the

probability for an event of each signature to be fully contained in the TeO_2 volume. We compute the containment efficiency ε_{MC} using Monte Carlo (MC) simulations (see Sec. IV) and expect it to be floor dependent. Specifically, in signatures (0) and (1) ε_{MC} should be larger for the uppermost and lowermost floors (floors 1 and 13) because these crystals only have neighbors on three sides rather than four, hence the γ rays have a higher chance of escaping undetected. Instead, signature (2), in which both γ rays are absorbed in the same crystal where the decay occurs, should have the same efficiency in all floors. Finally, we expect signatures (3), (4) and (5) to have a larger efficiency for $0\nu\beta^+EC$ decays taking place in the inner floors (2–12). Based on these considerations, we divide the data into subsets having the $0\nu\beta^+EC$ decay in floors 2–12 (subset 0) or floors 1,13 (subset 1). We give more details on the computation of the containment efficiency in Sec. IV.

We determine the energy resolution using the background peaks present in the CUORE-0 $M = 1$ physics spectrum, and keeping the distinction between floors 1, 13 and 2–12. We fit the most prominent peaks in the energy spectrum: the Annihilation Peak (AP) at 511 keV and the Single Escape Peak (SEP), plus a variety of γ lines ranging from 238 keV to 2615 keV. We find the AP and the SEP to be wider than the γ lines both in calibration and physics data. Signatures (3), (4) and (5) feature the annihilation peak in the signal parametrization, therefore we need to treat them separately from the γ lines. In signatures (1) and (4) a line at 1203.8 keV also appears in the signal parameterization: this line corresponds to the sum energy of the β^+ , the X-ray or Auger electron, and a 511 keV annihilation γ , hence it is also expected to be broadened.

We fit the energy resolution (σ) of the γ lines in the CUORE-0 physics spectrum as a function of energy with the following function:

$$\sigma_{\gamma}(E) = \sqrt{a + b \cdot E} \quad (3)$$

where a describes the thermal and electronic noise, while b is a parameter connected to the phonon production and collection. The fit results are reported in Table II. On the other hand, the presence in the physics spectrum of only two broadened peaks prevents a proper fit of energy resolution as a function of energy. Therefore we take σ_{B} , the resolution of the broadened lines, to be the average of the resolutions of the AP and SEP (Table II). The fits of σ_{γ} and σ_{B} for floors 2–12 are also shown in Fig. 2. This procedure differs from that used in Ref. [25] in the separation between floors 1–13 and 2–12, and in the ad-hoc treatment of the broadened lines.

The energy resolution of the signal peaks (see Eq. (9) of Sec. V) is taken as σ_{γ} or σ_{B} , depending on the presence of broadening in the considered signal. The same approach is used for the background components.

TABLE II. Best fit values for the parameters of Eq. (3), and σ_{B} of broadened peaks for subsets 0 and 1. The uncertainties correspond to the statistical errors of the fit.

d	a [keV ²]	b [keV]	σ_{B} [keV]
0	1.2(1)	$1.37(7) \cdot 10^{-3}$	2.1(2)
1	1.5(1)	$1.70(9) \cdot 10^{-3}$	2.4(2)

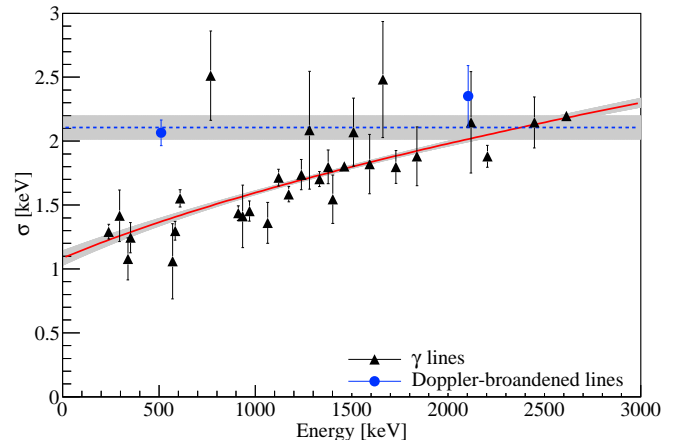


FIG. 2. Resolution curves for γ lines (black triangles, red solid curve) and broadened peaks (blue circles and blue dashed curve) for floors 2–12.

IV. MONTE CARLO SIMULATIONS

We use MC simulations to extract the containment efficiency, and to get an understanding of the most appropriate fit model for each signature. Specifically, we use the background model described in Ref. [26] to define a maximal fit model that contains, for each signature and subset, all components visible in the simulated spectra.

In order to compute the ^{120}Te $0\nu\beta^+EC$ decay containment efficiency, we simulated 10^7 positrons with 692.8 keV kinetic energy uniformly distributed in the TeO_2 volume. We define the containment efficiency ε_{MC} for a given signature and subset as the number of events which deposit energy in a $\pm 4\sigma$ window around the expected $0\nu\beta^+EC$ decay peak position $\bar{\mu}$, divided by the number of generated primaries:

$$\varepsilon_{\text{MC}} = \frac{N(E \in [\bar{\mu} - 4\sigma, \bar{\mu} + 4\sigma])}{N_{\text{tot}}} \quad (4)$$

We chose the number of generated primaries in order to have $\sigma_{\varepsilon_{\text{MC}}}/\varepsilon_{\text{MC}} \sim 1\%$. In all cases, we account for the non-operative channel in floor 10 [25]. For the signatures with $M > 1$ we also account for the live time fraction of the secondary channels.

Fig. 3 shows ε_{MC} for all $0\nu\beta^+EC$ decay signatures and for each single floor of CUORE-0. As discussed in Sec. III, the top and bottom floors feature different efficiencies for all signatures, except signature (2). In this

signature, all of the energy is deposited in a single crystal with no energy escaping, so the efficiency is unaffected by the detector geometry (see Fig. 1). The containment efficiency for each signature and subset is also reported in Table I.

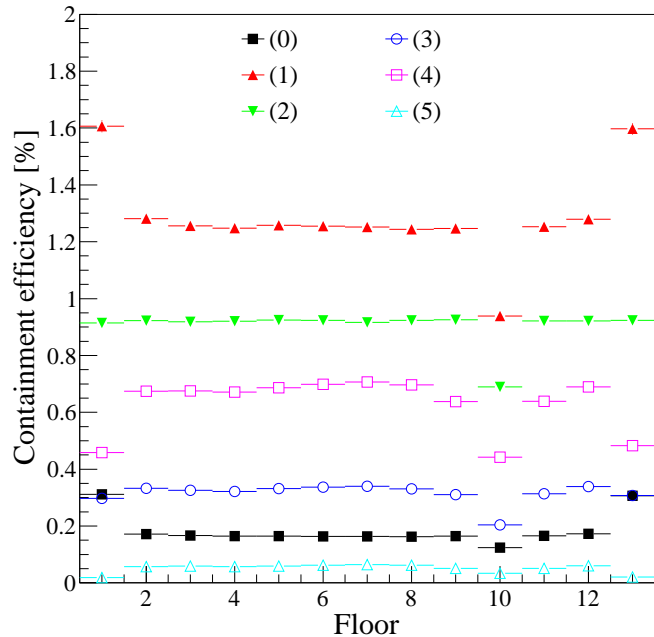


FIG. 3. Containment efficiency ε_{MC} for each floor and for all considered $0\nu\beta^+EC$ decay signatures. The uncertainty of the values is hidden by the markers. The efficiencies for signatures with $M > 1$ are corrected by the live time fraction of the secondary channels. All efficiencies of floors 9–11 are reduced because one of the detectors in floor 10 was not operative.

V. STATISTICAL APPROACH

We search for $0\nu\beta^+EC$ decay by means of a simultaneous unbinned Bayesian fit of the energy spectra of all signatures and subsets using the BAT software package [35]. The likelihood function is the product over the signatures (index s) and subsets (index d) of the unbinned (extended) terms:

$$\mathcal{L} = \prod_{s=0}^5 \prod_{d=0}^1 \frac{\lambda_{sd}^{n_{sd}} \cdot e^{-\lambda_{sd}}}{n_{sd}!} \prod_{i=1}^{n_{sd}} f(\vec{E}_{sdi} | \vec{\theta}_{sd}), \quad (5)$$

where n_{sd} is the number of events in the spectrum sd , λ_{sd} is the corresponding expectation value, f is the expected energy distribution of the signal and background events, \vec{E}_{sdi} represents the event energy values and $\vec{\theta}_{sd}$ are the model parameters. We drop the indexes s and d from here on where not necessary.

The expectation value λ is the sum of the expected number of signal events S , of linear background events B , and of events belonging to other possible background

components. For all signatures, we can consider the presence of additional background peaks in the vicinity of the $0\nu\beta^+EC$ decay peak position. We indicate these with an index p and a number of expected events P_p . Moreover, the signatures with multiplicity > 1 can feature the presence of additional background events distributed on horizontal, vertical or diagonal bands, as can be seen in Fig. 6. Namely, events in which a background γ undergoes a Compton scattering in one crystal and then is fully absorbed in a neighbor one, so that the two energy depositions sum up at the energy of the γ , are distributed on a diagonal band. On the other hand, a background γ can undergo a pair production followed by an electron-positron annihilation. If one of the 511 keV γ rays is absorbed in a neighbor crystal, while the other undergoes a Compton scattering within the original crystal and then escapes undetected, we measure a M2 event with 511 keV in the neighbor crystal and somewhat less than the energy of the SEP in the original one. Events of this type are distributed on a horizontal band. Finally, a background event can consist of two γ rays emitted in coincidence: if one is fully absorbed and the other undergoes a Compton scattering in a neighboring crystal and then escapes, the event lies in a vertical band. This can occur in ^{60}Co events, for example. We will refer to the horizontal/vertical bands with an index t (and expectation value T_t) and to the diagonal ones with an index q (and expectation value Q_q). The expectation value is therefore given by:

$$\lambda_{sd} = S_{sd} + B_{sd} + \sum_p P_{psd} + \sum_t T_{tsd} + \sum_q Q_{qsd} \quad (6)$$

For the background contributions we use the number of background events as a fit parameter, while for the signal contribution we express S as a function of the $0\nu\beta^+EC$ half-life:

$$S_{sd} = \frac{\ln 2}{T_{1/2}} \cdot \frac{N_A}{m_A} f_{120} \cdot \varepsilon_{sd} \cdot m_d \cdot t_d, \quad (7)$$

where N_A is the Avogadro number, m_A is the molar mass of TeO_2 , f_{120} is the ^{120}Te isotopic abundance, ε_{sd} is the total efficiency, i.e. the product of the containment efficiency $\varepsilon_{MC,sd}$, the coincidence efficiency for the considered signature multiplicity ε_M ($M = 1, 2, 3$) and the selection cut efficiency $\varepsilon_{\text{cut}}^\dagger$, while m_d and t_d are the TeO_2 mass and the measurement live time of subset d , respectively.

We model the energy distribution for every signature and subset according to the contributions considered in

[†] Notice that $\varepsilon_{MC,sd}$ is different for each signature and subset, ε_{Mi} depends on the event multiplicity for the considered signature, while ε_{cut} is common to all signatures and subsets.

Eq. (6). In general, we can express $f(\vec{E}|\vec{\theta})$ as:

$$\begin{aligned}
f(\vec{E}|\vec{\theta}) &= \frac{S}{\lambda} f_S(\vec{E}_i|\vec{\theta}) && \rightarrow \text{signal} \\
&+ \frac{B}{\lambda} f_B(\vec{E}_i|\vec{\theta}) && \rightarrow \text{linear background} \\
&+ \sum_p \frac{P_p}{\lambda} f_p(\vec{E}_i|\vec{\theta}) && \rightarrow \text{background peaks} \\
&+ \sum_t \frac{T_t}{\lambda} f_t(\vec{E}_i|\vec{\theta}) && \rightarrow \text{hor./vert. bands} \\
&+ \sum_q \frac{Q_q}{\lambda} f_q(\vec{E}_i|\vec{\theta}) && \rightarrow \text{diagonal bands.}
\end{aligned} \tag{8}$$

For all signatures, we parameterize the signal as an M -dimensional Gaussian distribution centered at the energies $\vec{\mu}$ reported in Table I:

$$f_S(\vec{E}_i|\vec{\theta}) = \prod_{r=1}^M \frac{1}{\sqrt{2\pi} \cdot \sigma_r} \exp\left[-\frac{(E_{ir} - \mu_r)^2}{2\sigma_r^2}\right], \tag{9}$$

where r is the dimension index running from 1 to the considered multiplicity M .

The distribution of background events depends both on the considered signature and subset. In general, we implement it as a linear distribution in all considered dimensions:

$$f_B(\vec{E}_i|\vec{\theta}) = \prod_{r=1}^M \left[\frac{1}{\Delta E_r} + \beta \cdot (E_{ir} - \hat{E}_r) \right], \tag{10}$$

where ΔE_r and \hat{E}_r are the fit range and its center, respectively, for the dimension index $r = 1, \dots, M$, while β is a parameter which describes the slope of the background distribution.

In case other background peaks are present in the fit region, we parameterize them as n -dimensional Gaussian peaks centered at energy $\vec{\mu}_p$ and with sigma $\vec{\sigma}_p$:

$$f_p(\vec{E}_i|\vec{\theta}) = \prod_{r=1}^M \frac{1}{\sqrt{2\pi} \cdot \sigma_{pr}} \exp\left[-\frac{(E_{ir} - \mu_{pr})^2}{2\sigma_{pr}^2}\right]. \tag{11}$$

The signatures with multiplicity > 1 can feature the presence of horizontal and/or vertical background bands, which we implement as:

$$f_t(\vec{E}_i|\vec{\theta}) = \frac{1}{\sqrt{2\pi}\sigma_t} \frac{1}{\Delta E_{|1-k|}} \exp\left[-\frac{(E_{ik} - \mu_t)^2}{2\sigma_t^2}\right], \tag{12}$$

where k is the index indicating the direction of the band in the 2-dimensional spectrum.

Finally, we fit the diagonal bands with:

$$f_q(\vec{E}_i|\vec{\theta}) = \frac{\exp\left[-\frac{(E_{i0}+E_{i1}-\mu_q)^2}{2\sigma_q^2}\right]}{\int_{\Delta E_1, \Delta E_2} \exp\left[-\frac{(E_{i0}+E_{i1}-\mu_q)^2}{2\sigma_q^2}\right] dE_1 dE_2}, \tag{13}$$

where E_{i0} and E_{i1} are the energies measured in the two crystals, μ_q is the energy of the original γ , and σ_q is the combination of the energy resolution in the two channels: $\sigma_q = \sqrt{\sigma_1^2 + \sigma_2^2}$.

The fit parameters with no prior information available are the normalization terms for the background contributions B_{sd} , P_{psd} , Q_{qsd} and T_{tsd} , and the parameter of interest is the $0\nu\beta^+EC$ inverse half-life, $1/T_{1/2}$. The nuisance parameters for which prior measurements are available are the containment efficiencies ε_{MC} , the coincidence cut efficiencies ε_M , the selection cut efficiency ε_{cut} , the ^{120}Te isotopic abundance f_{120} and the $0\nu\beta^+EC$ Q-value Q . The last three parameters and the inverse half-life are common to all signatures.

We use two sets of priors for the fit parameters. If an independent measurement is available for a parameter, we use a Gaussian prior centered at the measured value and with a σ equal to the corresponding uncertainty. This is the case for the efficiencies, Q and f_{120} . For all other parameters we use a flat prior in a range large enough to allow the corresponding marginalized posterior to go to zero, and bound to non-negative values if the considered parameter represents or is proportional to a number of counts. The choice of a flat prior does not influence significantly the posterior for the background components, because the information contained in the data is generally stronger than that provided by the prior. This is not true for the very small or negligible background components – with a posterior peaked at zero or compatible at 2σ with it – or $1/T_{1/2}$. In these cases, a log-flat prior, i.e. a prior flat in the logarithm of the variable, would yield a much stronger limit on the number of counts assigned to the considered background components, or on $1/T_{1/2}$. Therefore, the flat prior represents a conservative choice.

The inclusion of the energy resolution σ as a nuisance parameter would involve a further complication of the analysis software. Namely, while all other parameters can be either characteristic of each single fit component, or common to all of them (within the same signature and subset), the energy resolution is common to multiple background components of different signatures, and at the same time different background components of the same signature can have different resolutions. For sake of simplicity, we preferred to treat the energy resolution as a systematic effect and to run the analysis multiple times after shifting all σ values up and down by their uncertainties.

VI. RESULTS

We use the MC simulations [26] described in Sec. IV to define a maximal model containing all possible background contributions. We fit the maximal model to the data and iteratively remove those contributions for which the minimum of the 95% interval around the marginalized mode is zero. The only exception is made for the

linear background contribution, which we always keep in the fit. We denote the final fit model containing only the components with $> 2\sigma$ significance the “minimal model”. To better understand the relative importance of each signature and the effect of the nuisance parameters, we perform the fit on each signature separately, as well as on all of them together, and under the following conditions:

- with the minimal model and including the efficiencies, Q and f_{120} as nuisance parameters. This is our baseline approach;
- with the minimal model, keeping the efficiencies, Q and f_{120} fixed;
- with the maximal model and including the efficiencies, Q and f_{120} as nuisance parameters.

The background components of the minimal model for signatures (0)–(4) are shown in Figs. 5 and 6. These figures also show the best fit curves with the $0\nu\beta^+EC$ decay signal contribution normalized to the 90% credibility interval (CI) limit. Signature (5) has only 8 events hence we parameterize its background with a uniform distribution.

TABLE III. Results of the $0\nu\beta^+EC$ decay analysis on each individual signature, as well as on the combination of all signatures. We use the minimal model keeping the efficiencies, Q and f_{120} fixed (column “Less Pars.”), or considering them as nuisance parameters (column “All Pars.”). We consider the maximal model only in the case of signatures (2), (3), (4), and for the combination of all signatures. For signatures (0), (1) and (5) the maximal model is equivalent to the minimal model with additional nuisance parameters.

Signature	Limit on $T_{1/2}$ [yr]		Maximal All Pars.
	Less Pars.	All Pars.	
(0)	$2.8 \cdot 10^{19}$	$2.5 \cdot 10^{19}$	-
(1)	$1.6 \cdot 10^{20}$	$1.4 \cdot 10^{20}$	-
(2)	$4.7 \cdot 10^{20}$	$4.2 \cdot 10^{20}$	$4.2 \cdot 10^{20}$
(3)	$5.2 \cdot 10^{20}$	$4.4 \cdot 10^{20}$	$4.4 \cdot 10^{20}$
(4)	$1.2 \cdot 10^{21}$	$1.1 \cdot 10^{21}$	$1.1 \cdot 10^{21}$
(5)	$1.6 \cdot 10^{20}$	$1.5 \cdot 10^{20}$	-
All	$1.6 \cdot 10^{21}$	$1.6 \cdot 10^{21}$	$1.6 \cdot 10^{21}$

The results of all fits are reported in Table III. The inclusion of additional nuisance parameters for the efficiencies, Q and f_{120} weakens all limits by $\sim 10\%$, with the largest effect obtained for signature (2) and the greatest reduction coming from the uncertainty on f_{120} . The effect is not the same for all subsets: the reason comes from the presence of additional statistical fluctuations to which the fit becomes sensitive when Q is not constrained to its best fit value. When we run the fits simultaneously on all signatures, the inclusion of additional nuisance parameters affects the limit by just 1%. Additionally, the effect of the switch to the maximal model is at the percent level for all signatures, and indicates that the minimal model already provides an appropriate description

of the data.

Finally, we consider the uncertainty on the energy resolution as a systematic. We re-run the minimal model on the data with all efficiencies, Q and f_{120} as nuisance parameters and with the energy resolution increased or decreased by ± 1 standard deviation. This variation yields a $\mp 7\%$ change in the $T_{1/2}$ limit, respectively. With the described procedure we are neglecting all correlations between the uncertainties reported in Table II. Hence, this result represents a conservative estimation.

The fit of the minimal model on all signatures together with the inclusion of the efficiencies, Q and f_{120} as nuisance parameters, and without considering the systematic induced by energy resolution, gives a limit of

$$T_{1/2} > 1.6 \cdot 10^{21} \text{ yr} \quad (14)$$

for a 90% CI. The limit obtained with CUORE-0 data is slightly weaker than that achieved with Cuoricino. Specifically, the limit is weakened by the presence of a small upward fluctuation in signature (1), with significance of $\sim 1\sigma$.

We combine the results of CUORE-0 and Cuoricino through a Bayesian fit with a flat prior on $1/T_{1/2}$, rescaling the Cuoricino result to account for the corrected isotopic abundance. Thus, we obtain the strongest limit to date on $0\nu\beta^+EC$ decay of ^{120}Te :

$$T_{1/2} > 2.7 \cdot 10^{21} \text{ yr (90% CI)}, \quad (15)$$

with a 5% systematic uncertainty induced by the uncertainty on the CUORE-0 energy resolution. The $1/T_{1/2}$ posterior distribution for the combination of CUORE-0 and Cuoricino results is shown in Fig. 4.

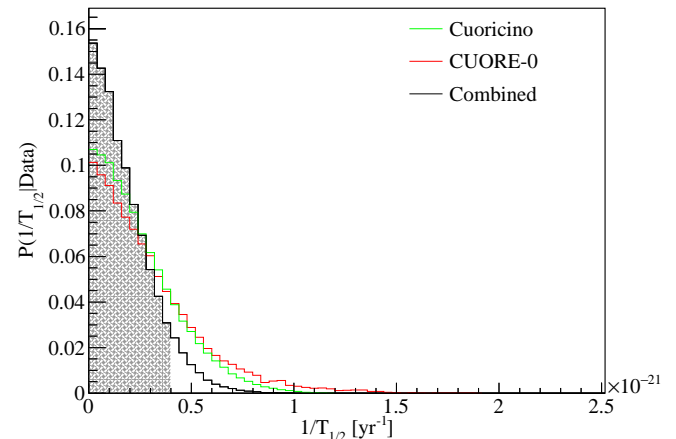


FIG. 4. Posterior distribution of $1/T_{1/2}$ obtained from Cuoricino (green), CUORE-0 (red), and their combination (black). The gray area corresponds to the 90% quantile.

VII. CONCLUSIONS

We performed a search of $0\nu\beta^+EC$ decay of ^{120}Te on CUORE-0 data. The lower background, the higher total

efficiency and the development of a dedicated fit which we can run simultaneously on multiple signatures with different multiplicities and on multiple data subsets allows us to reach a limit comparable to that of Cuoricino with approximately half the exposure. We can apply the analysis procedure developed for this work directly to CUORE data, once available, for the search of ^{120}Te $0\nu\beta^+EC$ decay and other physics processes, e.g. the $0\nu\beta\beta$ decay of ^{130}Te to excited states of ^{130}Xe , already studied with Cuoricino [36] and CUORE-0 [34]. The larger mass and higher containment efficiency for events with multiplicity > 1 could provide an increase of two orders of magnitude for all analyses of this kind.

ACKNOWLEDGMENTS

The CUORE Collaboration thanks the directors and staff of the Laboratori Nazionali del Gran Sasso and the technical staff of our laboratories. This work was supported by the Istituto Nazionale di Fisica Nucleare (INFN); the National Science Foundation under Grant Nos. NSF-PHY-0605119, NSF-PHY-0500337, NSF-PHY-0855314, NSF-PHY-0902171, NSF-PHY-0969852, NSF-PHY-1307204, NSF-PHY-1314881, NSF-PHY-1401832, and NSF-PHY-1404205; the Alfred P. Sloan Foundation; the University of Wisconsin Foundation; and Yale University. This material is also based upon work supported by the US Department of Energy (DOE) Office of Science under Contract Nos. DE-AC02-05CH11231, DE-AC52-07NA27344, and [de-sc0012654](#); and by the DOE Office of Science, Office of Nuclear Physics under Contract Nos. DE-FG02-08ER41551 and DE-FG03-00ER41138. This research used resources of the National Energy Research Scientific Computing Center (NERSC).

-
- [1] W. H. Furry, *Phys. Rev.* **56**, 1184 (1939).
- [2] S. Dell’Oro *et al.*, *Adv. High Energy Phys.* **2016**, 2162659 (2016), [arXiv:1601.07512](#).
- [3] M. Fukugita and T. Yanagida, *Phys. Lett.* **B174**, 45 (1986).
- [4] J. D. Vergados, H. Ejiri, and F. Simkovic, *Rept. Prog. Phys.* **75**, 106301 (2012), [arXiv:1205.0649](#).
- [5] C. Patrignani *et al.* (Particle Data Group), *Chin. Phys.* **C40**, 100001 (2016).
- [6] T. Kajita, *Rev. Mod. Phys.* **88**, 030501 (2016).
- [7] A. B. McDonald, *Rev. Mod. Phys.* **88**, 030502 (2016).
- [8] K. Eguchi *et al.* (KamLAND), *Phys. Rev. Lett.* **90**, 021802 (2003), [arXiv:hep-ex/0212021](#).
- [9] F. P. An *et al.* (Daya Bay), *Phys. Rev.* **D95**, 072006 (2017), [arXiv:1610.04802](#).
- [10] S. H. Seo *et al.* (RENO Collaboration), (2016), [arXiv:1610.04326](#).
- [11] R. Ardito *et al.* (CUORE Collaboration), (2005), [arXiv:hep-ex/0501010](#).
- [12] D. R. Artusa *et al.* (CUORE Collaboration), *Adv. High Energy Phys.* **2015**, 879871 (2015), [arXiv:1402.6072](#).
- [13] D. R. Artusa *et al.* (CUORE Collaboration), *Eur. Phys. J.* **C74**, 2956 (2014), [arXiv:1402.0922](#).
- [14] C. Alduino *et al.* (CUORE Collaboration), *JINST* **11**, P07009 (2016), [arXiv:1604.05465](#).
- [15] J. Meija *et al.*, *Pure Appl. Chem.* **88**, 293 (2016).
- [16] J. Barea, J. Kotila, and F. Iachello, *Phys. Rev.* **C87**, 057301 (2013), [arXiv:1509.05157](#).
- [17] J. Kotila, J. Barea, and F. Iachello, *Phys. Rev.* **C89**, 064319 (2014), [arXiv:1509.01927](#).
- [18] J. A. Bearden and A. F. Burr, *Rev. Mod. Phys.* **39**, 125 (1967).
- [19] N. D. Scielzo *et al.*, *Phys. Rev.* **C80**, 025501 (2009), [arXiv:0902.2376](#).
- [20] E. Andreotti *et al.* (Cuoricino Collaboration), *Astropart. Phys.* **34**, 643 (2011), [arXiv:1011.4811](#).
- [21] C. Arnaboldi *et al.* (Cuoricino Collaboration), *Phys. Lett.* **B584**, 260 (2004).
- [22] E. Buccheri, M. Capodiferro, S. Morganti, F. Orio, A. Pelosi, and V. Pettinacci, *Nucl. Instrum. Meth.* **A768**, 130 (2014), [arXiv:1405.0852](#).
- [23] F. Alessandria *et al.* (CUORE Collaboration), *Astropart. Phys.* **35**, 839 (2012), [arXiv:1108.4757](#).
- [24] F. Alessandria *et al.* (CUORE Collaboration), *Astropart. Phys.* **45**, 13 (2013), [arXiv:1210.1107](#).
- [25] K. Alfonso *et al.* (CUORE Collaboration), *Phys. Rev. Lett.* **115**, 102502 (2015), [arXiv:1504.02454](#).
- [26] C. Alduino *et al.* (CUORE Collaboration), *Eur. Phys. J.* **C77**, 13 (2017), [arXiv:1609.01666](#).
- [27] S. Y. F. Chu *et al.*, “The Lund/LBL Nuclear Data Search,” (1999).
- [28] E. Andreotti *et al.* (Cuoricino Collaboration), *Astropart. Phys.* **34**, 822 (2011), [arXiv:1012.3266](#).
- [29] C. Arnaboldi *et al.* (Cuoricino Collaboration), *Phys. Rev.* **C78**, 035502 (2008), [arXiv:0802.3439](#).
- [30] A. Alessandrello *et al.*, *Nucl. Instrum. Meth.* **B142**, 163 (1998).
- [31] C. Arnaboldi *et al.*, *Nucl. Instrum. Meth.* **A520**, 578 (2004).
- [32] C. Arnaboldi *et al.*, *Nucl. Instrum. Meth.* **A617**, 327 (2010).
- [33] C. Alduino *et al.* (CUORE Collaboration), *Phys. Rev.* **C93**, 045503 (2016).
- [34] S. Pozzi, *Search for double-beta decay of ^{130}Te to the excited states of ^{130}Xe in CUORE-0*, Ph.D. thesis, Università degli Studi di Milano-Bicocca (2017).
- [35] A. Caldwell, D. Kollar, and K. Kroninger, *Comput. Phys. Commun.* **180**, 2197 (2009), [arXiv:0808.2552](#).
- [36] E. Andreotti *et al.* (Cuoricino Collaboration), *Phys. Rev.* **C85**, 045503 (2012), [arXiv:1108.4313](#).

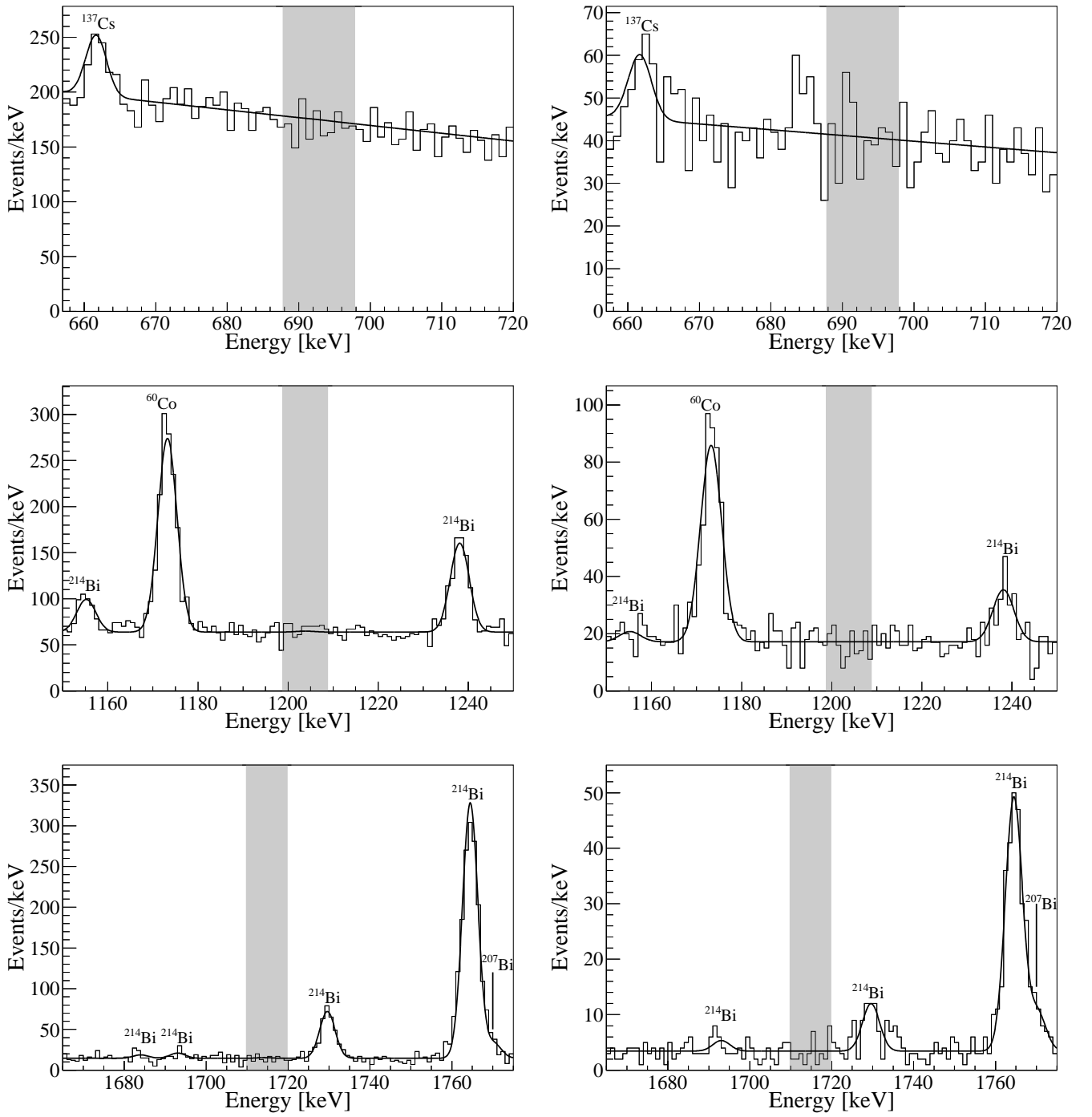


FIG. 5. Energy spectra for floors 2–12 (left) and 1,13 (right) relative to the signatures (0), (1) and (2) (top to bottom). The curves correspond to the best fit minimal model, with the $0\nu\beta^+EC$ decay peak normalized to the 90% CI limit. The shaded area corresponds to a 10 keV region around the expected signal peak position.

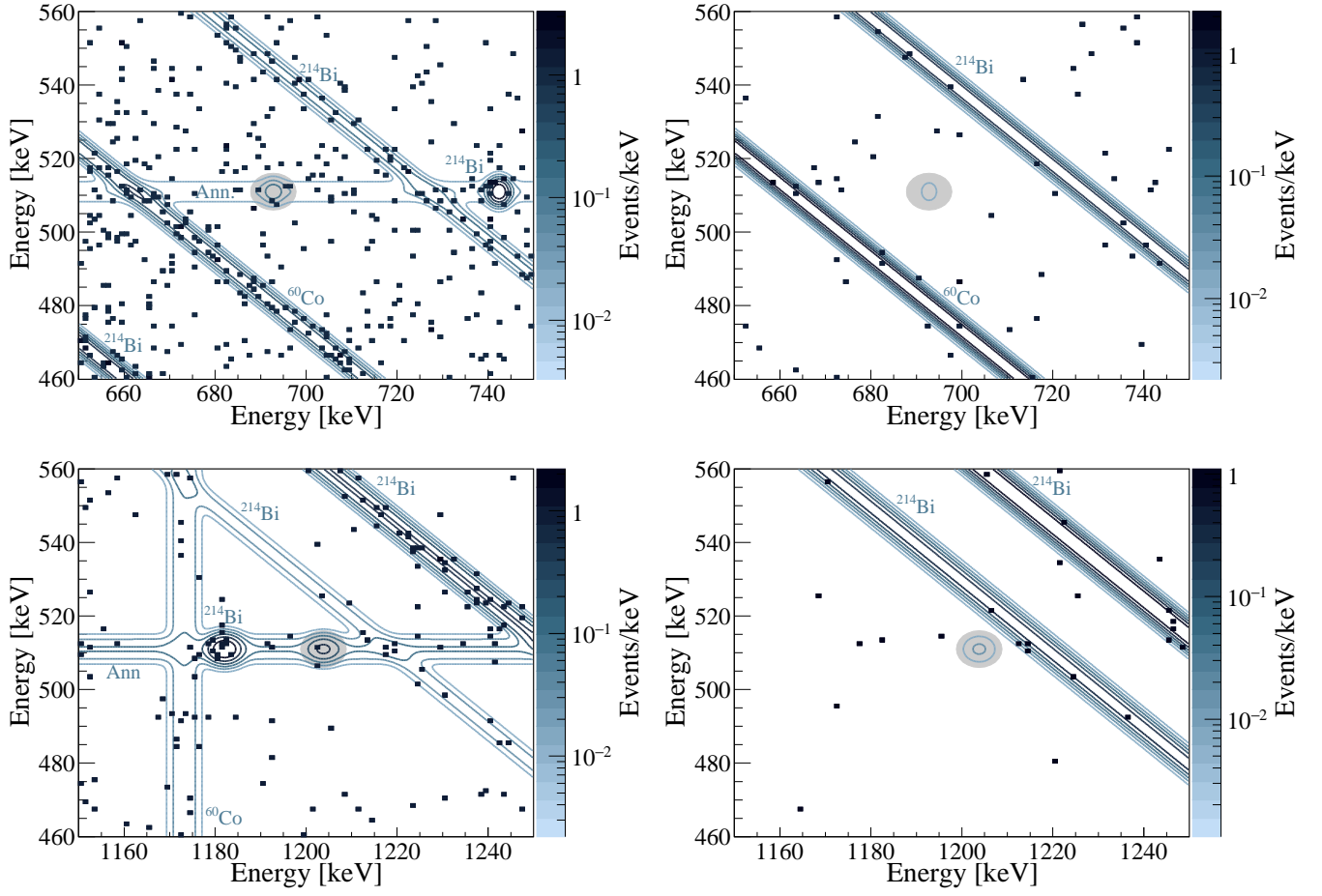


FIG. 6. Energy spectra for floors 2–12 (left) and 1,13 (right) relative to the signatures (3) and (4) (top to bottom). The squares correspond to the measured events. The contour curves correspond to the best fit minimal model, with the $0\nu\beta^+EC$ decay contribution normalized to the 90% CI limit. The shaded area corresponds to a 10 keV region around the expected signal peak position.